Chapter 3

# X-Ray N-Beam Takagi-Taupin Dynamical Theory and N-Beam Pinhole Topographs Experimentally Obtained and Computer-Simulated

Kouhei Okitsu, Yasuhiko Imai and Yoshitaka Yoda

Additional information is available at the end of the chapter

http://dx.doi.org/10.5772/47846

## 1. Introduction

In the field of X-ray crystal structure analysis, while the absolute values of structure factors are directly observed, phase information is lost in general. However, this problem (phase problem) has been overcome mainly by the direct method developed by Hauptmann and Karle except for protein crystals. In the case of protein crystal structure analysis, the isomorphous replacement method and/or anomalous dispersion method are mainly used to solve the phase problem. Phasing the structure factors is sometimes the most difficult process in protein crystallography.

On the other hand, It has been recognized for many years since the suggestion by Lipscomb in 1949 [12] that the phase information can be physically extracted, at least in principle, from X-ray diffraction profiles of three-beam cases in which transmitted and two reflected beams are simultaneously strong in the crystal. This suggestion was verified by Colella [3] that stimulated many authors [2, 4, 5, 21, 22] and let them investigate the multiple-beam ($n$-beam) method to solve the phase problem in protein crystallography.

The most primitive $n$-beam diffraction is the cases $n = 3$. The shape of three-beam rocking curve simply depends on the triplet phase invariant. In the case of protein crystallography, however, it is extremely difficult to realize such three-beam cases that transmitted and only two reflected beams are strong in the crystal, which is due to the extremely high density of reciprocal lattice nodes owing to the large size of unit cell of the crystal. Therefore, X-ray $n$-beam dynamical diffraction theory is necessary to solve the phase problem in protein crystallography. The Ewald-Laue (E-L) dynamical diffraction theory [7, 11] was extended to the three-beam cases in the late 1960's [8–10]. The numerical method to solve the $n$-beam ($n \geq 3$) E-L theory was given by Colella [3]. Colella's method [3] to solve the $n$-beam E-L theory is applicable only to the case of crystals with planar surfaces.

On the other hand, Okitsu and his coauthors [13, 14, 16, 17] extended the Takagi-Taupin (T-T) dynamical diffraction theory [18–20] to $n$-beam cases ($n \in \{3,4,5,6,8,12\}$) and presented a numerical method to solve the theory. They showed six-beam pinhole topographs experimentally obtained and computer-simulated based on the $n$-beam T-T equation, between which excellent agreements were found. In reference [16], it was shown that the $n$-beam T-T equation can deal with X-ray wave field in an arbitrary-shaped crystal.

In the $n$-beam method to solve the phase problem in the protein crystal structure analysis, one of the difficulty is the shape of the crystal which is complex in general. Then, the above advantage of $n$-beam T-T equation over the E-L dynamical theory is important. The present authors have derived an $n$-beam T-T equation applicable for arbitrary number of $n$, which will be published elsewhere.

The $n$-beam T-T equation was derived in references [13, 17] from Takagi's fundamental equation of the dynamical theory [19]. In section 2 of the present chapter, however, the $n$-beam E-L theory is described at first. The $n$-beam T-T equation is derived by Fourier-transforming the $n$-beam E-L dynamical theory. Then, it is also described that the E-L theory can be derived from the T-T equation. This reveals a simple relation between the E-L and T-T formulations of X-ray dynamical diffraction theory. This equivalence between the E-L and T-T formulations has been implicitly recognized for many years but is explicitly described for the first time. In section 5, experimentally obtained and computer-simulated pinhole topographs are shown for $n \in \{3,4,5,6,8,12\}$, which verifies the theory and the computer algorithm to solve it.

## 2. Derivation of the $n$-beam Takagi-Taupin equation

### 2.1. Description of the $n$-beam Ewald-Laue dynamical diffraction theory

The fundamental equation with the E-L formulation is given by [1, 2]

$$\frac{k_i^2 - K^2}{k_i^2}\boldsymbol{\mathcal{D}}_i = \sum \chi_{h_i - h_j} \left[\boldsymbol{\mathcal{D}}_j\right]_{\perp \mathbf{k}_i}. \tag{1}$$

Here, $k_i$ is wavenumber of the $i$th numbered Bloch wave whose wave vector is $\mathbf{k}_0 + \mathbf{h}_i$ where $\mathbf{k}_0$ is the wave vector of the forward-diffracted wave in the crystal, $K(= 1/\lambda)$ is the wavenumber of X-rays in vacuum, $\boldsymbol{\mathcal{D}}_i$ and $\boldsymbol{\mathcal{D}}_j$ are complex amplitude vectors of the $i$th and $j$th numbered Bloch waves, $\sum$ is an infinite summation for all combinations of $i$ and $j$, $\chi_{h_i - h_j}$ is Fourier coefficient of electric susceptibility and $[\boldsymbol{\mathcal{D}}_j]_{\perp \mathbf{k}_i}$ is component vector of $\boldsymbol{\mathcal{D}}_j$ perpendicular to $\mathbf{k}_i$, respectively.

By applying an approximation that $k_i + K \approx 2k_i$ to (1), the following equation is obtained,

$$\xi_i \boldsymbol{\mathcal{D}}_i = \frac{K}{2} \sum \chi_{h_i - h_j} \left[\boldsymbol{\mathcal{D}}_j\right]_{\perp \mathbf{k}_i}, \quad \text{where } \xi_i = k_i - K. \tag{2}$$

Let the electric displacement vector $\boldsymbol{\mathcal{D}}_i$ be represented by a linear combination of scalar amplitudes as follows:

$$\boldsymbol{\mathcal{D}}_i = \mathcal{D}_i^{(0)} \mathbf{e}_i^{(0)} + \mathcal{D}_i^{(1)} \mathbf{e}_i^{(1)}.$$

Here, $\mathbf{e}_i^{(0)}$ and $\mathbf{e}_i^{(1)}$ are unit vectors perpendicular to $\mathbf{s}_i$, where $\mathbf{s}_i$ is a unit vector parallel to $\mathbf{k}_i$. $\mathbf{s}_i$, $\mathbf{e}_i^{(0)}$ and $\mathbf{e}_i^{(1)}$ construct a right-handed orthogonal system in this order. (2) can be described as follows:

$$\begin{aligned}\xi \cos\Theta_B \mathcal{D}_i^{(l)} &= -K\left(S_{i,0}^{(0)}\beta^{(0)} + S_{i,0}^{(1)}\beta^{(1)}\right)\mathcal{D}_i^{(l)} \\ &\quad + \frac{K}{2}\sum_{j=0}^{n-1}\sum_{m=0}^{1} C_{i,j}^{(l,m)}\chi_{h_i-h_j}\mathcal{D}_j^{(m)}, \\ &\text{where,} \quad i,j \in \{0,1,\cdots,n-1\}, n \in \{3,4,5,6,8,12\}, \\ &\quad\ \ l,m \in \{0,1\}.\end{aligned} \tag{3}$$

Here, $S$ and $C$ are polarization factors defined by

$$\mathbf{e}_j^{(m)} = S_{i,j}^{(m)}\mathbf{s}_i + C_{i,j}^{(0,m)}\mathbf{e}_i^{(0)} + C_{i,j}^{(1,m)}\mathbf{e}_i^{(1)}, \tag{4}$$

where $i$ and $j$ are ordinal numbers of waves ($i,j \in \{0,1,2,\cdots,n-1\}$) and $l$ and $m$ are ordinal numbers of polarization state ($l,m \in \{0,1\}$). When deriving (3) from (2), all reciprocal lattice nodes lying on the surface of Ewald sphere are assumed to be on a circle in reciprocal space. Then number of waves $n$ are limited to be $n \in \{3,4,5,6,8,12\}$ even in the case of cubic crystals with the highest symmetry. $\Theta_B$ is the angle spanned by $\overrightarrow{PQ}$ and $\mathbf{k}_i$ which is an identical value for every $i$ ($i \in \{0,1,2,\cdots,n-1\}$), where $P$ and $Q$ are centers of the Ewald sphere and the circle on which the reciprocal lattice nodes lie, respectively. $\xi$ is such a value that

$$\overrightarrow{P_1P_1'} = -\xi\overrightarrow{PQ}/\left|\overrightarrow{PQ}\right|, \tag{5}$$

where $P_1'$ is the common initial point of $\mathbf{k}_i$ [whose terminal points are $H_i$ ($i \in \{0,1,\cdots,n-1\}$)] and $P_1$ is a point on the sphere whose distance from the origin $O$ of reciprocal space is $K$. Hereafter, this surface of sphere is approximated as a plane whose distance from $O$ is $K$ in the vicinity of the Laue point $La$ whose distance from $H_i$ ($i \in \{0,1,\cdots,n-1\}$) is the identical value $K$. For description in the next section, it is described here that $\overrightarrow{P_1P_1'}$ is represented by a linear combination of $\mathbf{s}_i$, $\mathbf{e}_i^{(0)}$ and $\mathbf{e}_i^{(1)}$ as follows:

$$\overrightarrow{P_1P_1'} = -\xi\left(\cos\Theta_B\mathbf{s}_i + \eta_i^{(0)}\sin\Theta_B\mathbf{e}_i^{(0)} + \eta_i^{(1)}\sin\Theta_B\mathbf{e}_i^{(1)}\right).$$

$P_1$ is such a point that

$$\overrightarrow{P_1La} = K\left(\beta^{(0)}\mathbf{e}_0^{(0)} + \beta^{(1)}\mathbf{e}_0^{(1)}\right). \tag{6}$$

(2) and (3) can also be represented using matrices and vector as follows:

$$\xi\cos\Theta_B\mathbf{E}\boldsymbol{\mathcal{D}} = \mathbf{A}\boldsymbol{\mathcal{D}}. \tag{7}$$

Here, $\mathbf{E}$ is a unit matrix of size $2n$, $\boldsymbol{\mathcal{D}}$ is a amplitude column vector of size $2n$ whose $q$th element is $D_j^{(m)}$ $(q = 2j + m + 1)$ and $\mathbf{A}$ is a square matrix of size $2n$ whose element $a_{p,q}$ is given by

$$a_{p,q} = \frac{K}{2}\chi_{h_i - h_j} C_{i,j}^{(l,m)} - \delta_{p,q} K \left( S_{i,0}^{(0)} \beta^{(0)} + S_{i,0}^{(1)} \beta^{(1)} \right).$$

Here, $p = 2i + l + 1$ and $\delta_{p,q}$ is Kronecker delta. $2n$ couples of $\xi$ and $\boldsymbol{\mathcal{D}}$ can be obtained by solving eigenvalue-eigenvector problem of (7). This problem was solved by Colella [3] for the first time. Dispersion surfaces on which the initial point $P_1'$ of wave vectors of Bloch waves should be, is given as $2n$ sets of eigenvalues for (7).

## 2.2. Derivation of the $n$-beam Takagi-Taupin equation from the Ewald-Laue theory

In this section, the $n$-beam theory of T-T formulation is derived by Fourier-transforming the $n$-beam E-L theory described by (3).

A general solution of dynamical diffraction theory is considered to be coherent superposition of Bloch plane-wave system when X-ray wave field $\tilde{\mathbf{D}}(\mathbf{r})$ is given as follows:

$$\tilde{\mathbf{D}}(\mathbf{r}) = \sum_{i=0}^{n-1} \sum_{l=0}^{1} \mathbf{e}_i^{(l)} D_i^{(l)}(\mathbf{r}) \exp\left( -\mathrm{i}2\pi \overrightarrow{LaH_i} \cdot \mathbf{r} \right), \tag{8}$$

where $\mathbf{r}$ is the location vector. For the following description, $\mathbf{r}$ is described by a linear combination of $\mathbf{s}_i$, $\mathbf{e}_i^{(0)}$ and $\mathbf{e}_i^{(1)}$ as follows,

$$\mathbf{r} = s_i \mathbf{s}_i + e_i^{(0)} \mathbf{e}_i^{(0)} + e_i^{(1)} \mathbf{e}_i^{(1)}. \tag{9}$$

The amplitude of the $i$th component wave whose polarization state is $l$ is described as,

$$\mathcal{D}_i^{(l)}(\Delta\mathbf{k}) \exp\left( -\mathrm{i}2\pi \overrightarrow{P_1'H_i} \cdot \mathbf{r} \right) = \mathcal{D}_i^{(l)}(\Delta\mathbf{k}) \exp\left( -\mathrm{i}2\pi \Delta\mathbf{k} \cdot \mathbf{r} \right) \exp\left( -\mathrm{i}2\pi \overrightarrow{LaH_i} \cdot \mathbf{r} \right),$$
$$\text{where } \Delta\mathbf{k} = \overrightarrow{P_1'La}.$$

In this section, the amplitude of plane wave whose wave vector is $\mathbf{k}_i$ and polarization state is $l$ is denoted by $\mathcal{D}_i^{(l)}(\Delta\mathbf{k})$ in place of $\mathcal{D}_i^{(l)}$ in order to clarify this value depends on $\Delta\mathbf{k}$. $D_i^{(l)}(\mathbf{r})$ in (8) is represented by superposing coherently $\mathcal{D}_i^{(l)}(\Delta\mathbf{k})$ as follows:

$$D_i^{(l)}(\mathbf{r}) = \int_{\Delta\mathbf{k}}^{D.S.} \mathcal{D}_i^{(l)}(\Delta\mathbf{k}) \exp\left( -\mathrm{i}2\pi \Delta\mathbf{k} \cdot \mathbf{r} \right) \mathrm{d}S_k. \tag{10}$$

Substituting (4) with $j = 0$, (5), (6) and (9) into (10),

$$D_i^{(l)}(\mathbf{r}) = \int_{\Delta\mathbf{k}}^{D.S.} \mathcal{D}_i^{(l)}(\Delta\mathbf{k}) \times \exp\left\{ -\mathrm{i}2\pi \left[ \left( \xi \cos\Theta_B + K\beta^{(0)} S_{i,0}^{(0)} + K\beta^{(1)} S_{i,0}^{(1)} \right) s_i + T_i(\xi, e_i^{(0)}, e_i^{(1)}) \right] \right\} \mathrm{d}S_k. \tag{11}$$

Here, $\int_{\Delta k}^{D.S.} \mathrm{d}S_k$ means an integration over the dispersion surfaces in reciprocal space and $T_i(\xi, e_i^{(0)}, e_i^{(1)})$ is a term that does not depend on $s_i$. $\partial D_i^{(l)}(\mathbf{r})/\partial s_i$ can be calculated as follows:

$$\begin{aligned}\frac{\partial}{\partial s_i} D_i^{(l)}(\mathbf{r}) &= \frac{\partial}{\partial s_i} \int_{\Delta\mathbf{k}}^{D.S.} \mathcal{D}_i^{(l)}(\Delta\mathbf{k}) \exp\left(-\mathrm{i}2\pi\Delta\mathbf{k}\cdot\mathbf{r}\right) \mathrm{d}S_k \\ &= \int_{\Delta\mathbf{k}}^{D.S.} \frac{\partial}{\partial s_i} \left[\mathcal{D}_i^{(l)}(\Delta\mathbf{k}) \exp\left(-\mathrm{i}2\pi\Delta\mathbf{k}\cdot\mathbf{r}\right)\right] \mathrm{d}S_k \\ &= -\mathrm{i}2\pi \int_{\Delta\mathbf{k}}^{D.S.} \left[\xi\cos\Theta_B + K\left(S_{i,0}^{(0)}\beta^{(0)} + S_{i,0}^{(1)}\beta^{(1)}\right)\right] \mathcal{D}_i^{(l)}(\Delta\mathbf{k}) \exp\left(-\mathrm{i}2\pi\Delta\mathbf{k}\cdot\mathbf{r}\right) \mathrm{d}S_k. \end{aligned} \tag{12}$$

Substituting (3) into (12),

$$\begin{aligned}\frac{\partial}{\partial S_i} D_i^{(l)}(\mathbf{r}) &= -\mathrm{i}\pi K \int_{\Delta\mathbf{k}}^{D.S.} \sum_{j=0}^{n-1} \sum_{m=0}^{1} C_{i,j}^{(l,m)} \chi_{h_i - h_j} \mathcal{D}_j^{(m)}(\Delta\mathbf{k}) \exp\left(-\mathrm{i}2\pi\Delta\mathbf{k}\cdot\mathbf{r}\right) \mathrm{d}S_k \\ &= -\mathrm{i}\pi K \sum_{j=0}^{n-1} \sum_{m=0}^{1} C_{i,j}^{(l,m)} \chi_{h_i - h_j} \int_{\Delta\mathbf{k}}^{D.S.} \mathcal{D}_j^{(m)}(\Delta\mathbf{k}) \exp\left(-\mathrm{i}2\pi\Delta\mathbf{k}\cdot\mathbf{r}\right) \mathrm{d}S_k. \end{aligned} \tag{13}$$

Incidentally, when the crystal is perfect, the electric susceptibility $\chi(\mathbf{r})$ is represented by Fourier series as $\chi(\mathbf{r}) = \sum_{\mathbf{h}_i} \chi_{h_i} \exp[-\mathrm{i}2\pi\mathbf{h}_i\cdot\mathbf{r}]$. However, when the crystal has a lattice displacement field of $\mathbf{u}(\mathbf{r})$, the electric susceptibility is approximately given by $\chi[\mathbf{r}-\mathbf{u}(\mathbf{r})]$ and represented by Fourier series as follows,

$$\chi[\mathbf{r}-\mathbf{u}(\mathbf{r})] = \sum_{\mathbf{h}_i} \chi_{h_i} \exp[\mathrm{i}2\pi\mathbf{h}_i\cdot\mathbf{u}(\mathbf{r})] \exp(-\mathrm{i}2\pi\mathbf{h}_i\cdot\mathbf{r}).$$

Then, in the case of crystal with a lattice displacement field of $\mathbf{u}(\mathbf{r})$, $\chi_{h_i-h_j}$ can be replaced by $\chi_{h_i-h_j} \exp[\mathrm{i}2\pi(\mathbf{h}_i-\mathbf{h}_j)\cdot\mathbf{u}(\mathbf{r})]$. Therefore, the following equation is obtained from (13),

$$\frac{\partial}{\partial s_i} D_i^{(l)}(\mathbf{r}) = -\mathrm{i}\pi K \sum_{j=0}^{n-1} \sum_{m=0}^{1} C_{i,j}^{(l,m)} \chi_{h_i-h_j} \exp\left[\mathrm{i}2\pi(\mathbf{h}_i-\mathbf{h}_j)\cdot\mathbf{u}(\mathbf{r})\right] D_j^{(m)}(\mathbf{r}), \tag{14}$$

where, $i, j \in \{0, 1, \cdots, n-1\}, n \in \{3, 4, 5, 6, 8, 12\}$,

$l, m \in \{0, 1\}$.

The above equation is nothing but the $n$-beam T-T equation that appeared as eq. (4) in reference [17].

### 2.3. Derivation of the $n$-beam E-L dynamical theory from the T-T equation

In this section, it is described that the $n$-beam E-L theory given by (3) can be derived from the $n$-beam T-T equation (14).

When plane-wave X-rays are incident on the crystal to excite $2n$ tie points on the dispersion surfaces, each Bloch plane-wave system is described by

$$\tilde{\boldsymbol{\mathcal{D}}} = \sum_{i=0}^{n-1} \sum_{l=0}^{1} \mathbf{e}_i^{(l)} \mathcal{D}_i^{(l)} \exp\left(-\mathrm{i}2\pi\Delta\mathbf{k}\cdot\mathbf{r}\right) \exp\left(-\mathrm{i}2\pi\overrightarrow{LaH_i}\cdot\mathbf{r}\right).$$

Even when $D_i^{(l)}(\mathbf{r}) = \mathcal{D}_i^{(l)} \exp(-\mathrm{i}2\pi\mathbf{k}_i^{(l)}\cdot\mathbf{r})$, $D_i^{(l)}(\mathbf{r})$ should satisfy (14) with $\mathbf{u}(\mathbf{r}) = 0$,

$$\frac{\partial}{\partial s_i}\left[\mathcal{D}_i^{(l)} \exp\left(-\mathrm{i}2\pi\Delta\mathbf{k}\cdot\mathbf{r}\right)\right] = -\mathrm{i}\pi K \sum_{j=0}^{n-1} \sum_{m=0}^{1} C_{i,j}^{(l,m)} \chi_{h_i-h_j} \left[\mathcal{D}_j^{(m)} \exp\left(-\mathrm{i}2\pi\Delta\mathbf{k}\cdot\mathbf{r}\right)\right]. \quad (15)$$

Applying the same procedure as used when deriving (11),

$$\begin{aligned}
&\frac{\partial}{\partial s_i}\left[\mathcal{D}_i^{(l)} \exp\left(-\mathrm{i}2\pi\Delta\mathbf{k}\cdot\mathbf{r}\right)\right] \\
&= \mathcal{D}_i^{(l)} \frac{\partial}{\partial s_i} \exp\left\{-\mathrm{i}2\pi\left[\left(\xi\cos\Theta_B + K\beta^{(0)}S_{i,0}^{(0)} + K\beta^{(1)}S_{i,0}^{(1)}\right)s_i + T_i(\xi, e_i^{(0)}, e_i^{(1)})\right]\right\} \\
&= -\mathrm{i}2\pi\left(\xi\cos\Theta_B + K\beta^{(0)}S_{i,0}^{(0)} + K\beta^{(1)}S_{i,0}^{(1)}\right)\left[\mathcal{D}_i^{(l)} \exp\left(-\mathrm{i}2\pi\Delta\mathbf{k}\cdot\mathbf{r}\right)\right]. \quad (16)
\end{aligned}$$

Comparing (15) and (16), the same equation as (3) is obtained. The equivalence between the $n$-beam E-L and T-T X-ray dynamical diffraction theories ($n \in \{3,4,5,6,8,12\}$) described by a Fourier transform as defined by (10) is verified. As far as the present authors know, description on this equivalence between the E-L and T-T dynamical diffraction theories for two-beam case is found just in section 11.3 of Authier's book [1].

## 3. Algorithm to solve the theory

Figure 1($a$) and 1($b$) are schematic drawings for explanation of the algorithm to solve the $n$-beam T-T equation (14) for a six-beam case whose computer-simulated and experimentally obtained results are shown in Figure 9 of the present chapter. Vectors $\overrightarrow{R_i^{(0)}R^{(1)}}$ in Figure 1($a$) are parallel to $\mathbf{s}_i$. When the length of $\overrightarrow{R_i^{(0)}R^{(1)}}$ is sufficiently small compared with the extinction length $-1/(\chi_0 K)$ of the forward diffraction, The T-T equation (14) can be approximated by

$$\begin{aligned}
&\frac{D_i^{(l)}(R^{(1)}) - D_i^{(l)}(R_i^{(0)})}{\left|\overrightarrow{R_i^{(0)}R^{(1)}}\right|} \\
&= -\mathrm{i}\pi K \sum_{j=0}^{n-1} \sum_{m=0}^{1} \left\{\chi_{h_i-h_j} \exp\left[\mathrm{i}2\pi\left(\mathbf{h}_i - \mathbf{h}_j\right)\cdot\mathbf{u}(Rm_i)\right]\right. \\
&\quad \left.\times C_{i,j}^{(l,m)}\left[D_j^{(m)}(R_i^{(0)}) + D_j^{(m)}(R^{(1)})\right]/2\right\}. \quad (17)
\end{aligned}$$

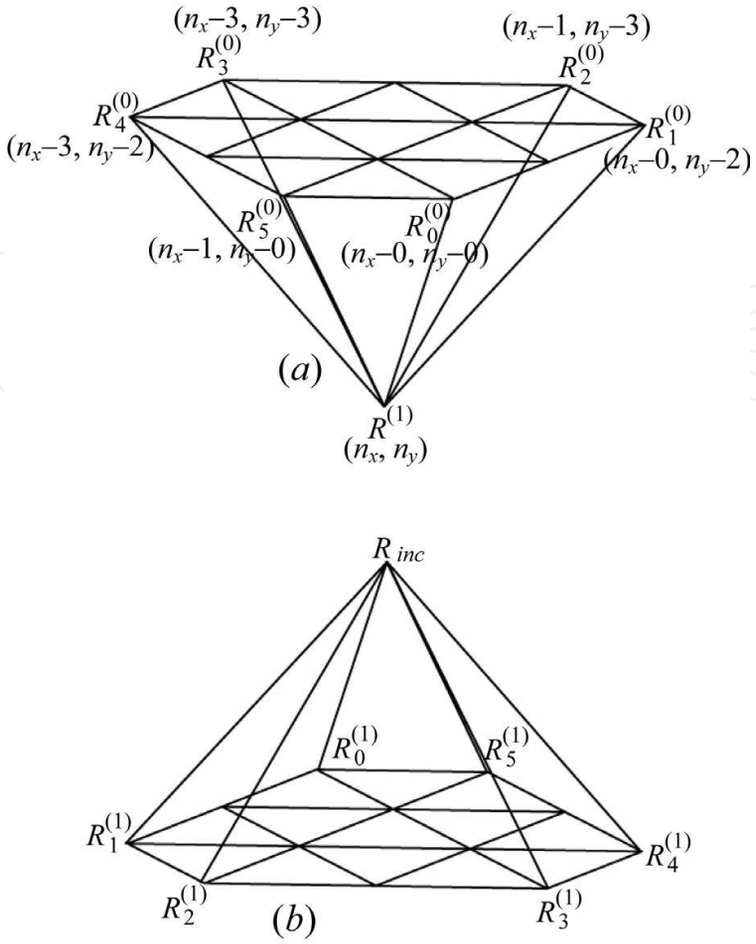


**Figure 1.** This Figure shows small hexagonal pyramids used when solving the T-T equation (14) in a six-beam case whose results are shown in Figure 9.

The above equation (17) can be described using matrix and vectors as follows:

$$\mathbf{A} = \mathbf{BD} \tag{18}$$

$$\text{where, } a_p = -\mathrm{i}\frac{1}{2}\pi K \sum_{j=0}^{n-1}\sum_{m=0}^{1} \chi_{h_i-h_j} \exp\left[\mathrm{i}2\pi(\mathbf{h}_i-\mathbf{h}_j)\cdot\mathbf{u}(Rm_i)\right] C_{i,j}^{(l,m)} D_j^{(m)}(R_i^{(0)}) + \frac{D_i^{(l)}(R_i^{(0)})}{\left|\overrightarrow{R_i^{(0)}R^{(1)}}\right|},$$

$$b_{p,q} = \mathrm{i}\frac{1}{2}\pi K \chi_{h_i-h_j} \exp\left[\mathrm{i}2\pi(\mathbf{h}_i-\mathbf{h}_j)\cdot\mathbf{u}(Rm_i)\right] C_{i,j}^{(l,m)} + \frac{\delta_{p,q}}{\left|\overrightarrow{R_i^{(0)}R^{(1)}}\right|},$$

$$d_q = D_j^{(m)}(R^{(1)}),$$

$$p = 2i + l + 1,$$

$$q = 2j + m + 1.$$

Here, **A** and **D** are column vectors of size $2n$ whose $p$th and $q$th elements are $a_p$ and $d_q$, respectively, and **B** is a square matrix of size $2n$ whose element of the $p$th column and the $q$th raw is $b_{p,q}$.

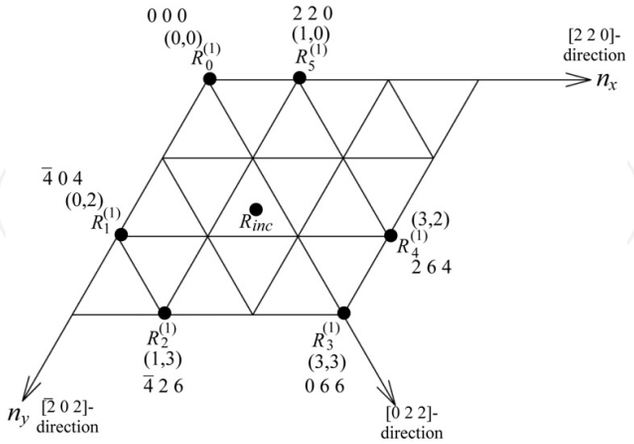


**Figure 2.** This Figure shows a top view of Figure $1(b)$.

Figure 2 is a top view of Figure $1(b)$. The X-ray amplitudes $D_j^{(m)}(R_i^{(1)})$ were calculated from the X-ray amplitudes at the incidence point $D_0^{(l)}(R_{inc})$ of the crystal surface. In this case, 0 0 0-forward-diffracted and $\overline{4}$ 0 4-, $\overline{4}$ 2 6-, 0 6 6-, 2 6 4- and 2 2 0-reflected X-rays are simultaneously strong. The angle spanned by $n_x$- and $n_y$-axes is 120°. $\overrightarrow{R_{inc}R_i^{(1)}}$ in Figure $1(b)$ are parallel to the wave vectors of 0 0 0-forward-diffracted and $\overline{4}$ 0 4-, $\overline{4}$ 2 6-, 0 6 6-, 2 6 4- and 2 2 0-reflected X-rays. As a boundary condition on the crystal surface, amplitude array $D_{even}(i,l,n_x,n_y)$ has nonzero value (unity) when $(i,l,n_x,n_y)$=(0,0,0,0) or $(i,l,n_x,n_y)$=(0,1,0,0). On the first layer, nonzero X-ray amplitudes $D_{odd}(j,m,n_x,n_y)$ are calculated when $(n_x,n_y) = [n'_x(i),n'_y(i)]$ $(i \in \{0,1,\cdots,n-1\})$. Here, $[n'_x(i),n'_y(i)] = (0,0),(0,2),(1,3),(3,3),(3,2)$ and $(1,0)$ for $i = 0$, 1, 2, 3, 4, 5, respectively. In general, $D_{even}(i,l,n_x,n_y)$ [or $D_{odd}(i,l,n_x,n_y)$] is calculated as $D_i^{(l)}(R^{(1)})$ by substituting $D_{odd}(j,m,n_x - n'_x(i),n_y - n'_y(i))$ [or $D_{even}(j,m,n_x - n'_x(i),n_y - n'_y(i))$] into $D_j^{(m)}(R_i^{(0)})$ in (17). The calculation was performed layer by layer scanning $n_x$ and $n_y$ in a range of $NMin[n'_x(i)] \le n_x \le N\,Max[n'_x(i)]$ and $NMin[n'_y(i)] \le n_y \le N\,Max[n'_y(i)]$, where $N$ is the ordinal number of layer. The values of $\chi_{h_i-h_j}$ were calculated by using *XOP* version 2.3 [6].

## 4. Experimental

### 4.1. Phase-retarder system

When taking four-, five-, six- and eight-beam pinhole topographs shown in section 5, the horizontally polarized synchrotron X-rays monochromated to be 18.245 keV with a water-cooled diamond monochromator system at BL09XU of SPring-8 were incident on the 'rotating four-quadrant phase retarder system' [15, 17].

Figure 3 shows $(a)$ a schematic drawing of the phase retarder system and $(b)$ a photograph of it. [1 0 0]-oriented four diamond crystals $PR_n$ $(n \in \{1,2,3,4\})$ with thicknesses of 1.545,

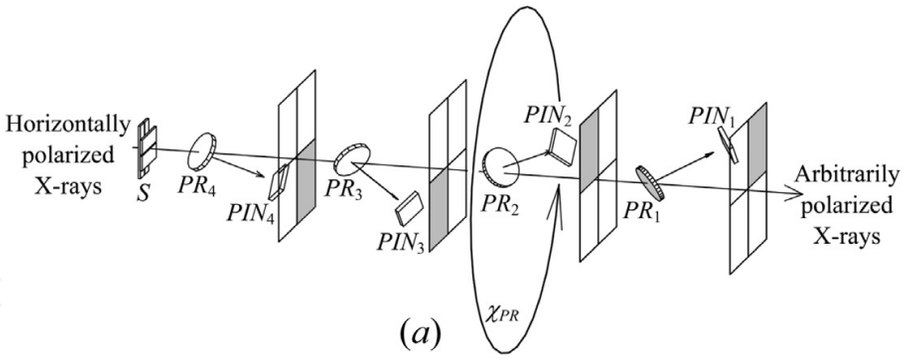


(a)

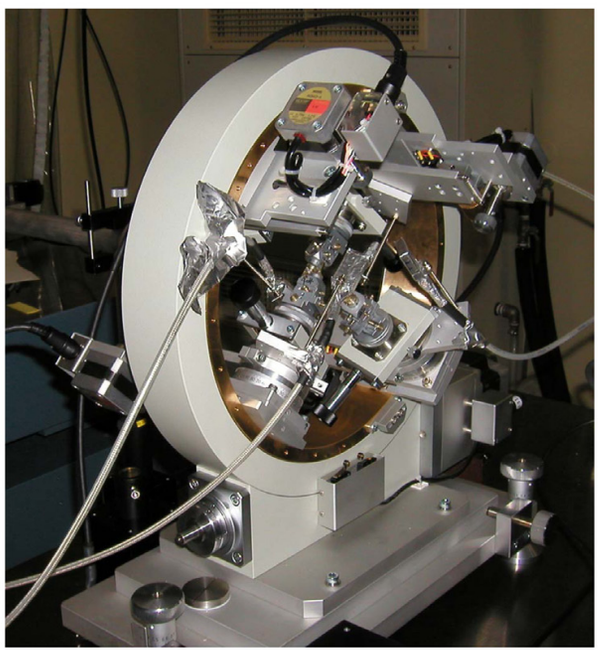

(b)

**Figure 3.** $(a)$ is a schematic drawing of the 'rotating four-quadrant phase retarder system' (reproduction of Figure 3 in reference [17]). $(b)$ is a photograph of it.

2.198, 1.565 and 2.633 mm were mounted on tangential-bar type goniometers such that the deviation angles $\Delta\theta_{PR_n}$ from the exact Bragg condition of 1 1 1 reflection in an asymmetric Laue geometry can be controlled. See Figure 4 in reference [17] for more detail. The four tangential-bar type goniometers were mounted in a $\chi$-circle goniometer [see Figure 3 $(b)$] such that the whole system of the phase retarders can be rotated around the beam axis of transmitted X-rays. The rotation angle of the $\chi$-circle $\chi_{PR}$ and $\Delta\theta_{PR_n}$ were controlled as summarized in Table 3 in reference [17] such that horizontal-linearly (LH), vertical-linearly (LV), right-screwed circularly (CR), left-screwed circularly (CL), $-45°$-inclined-linearly (L$-$45) and $+45°$-inclined-linearly (L$+$45) polarized X-rays were generated to be incident on the sample crystal.

In the cases of three- and twelve-beam pinhole topographs, horizontally polarized synchrotron X-rays monochromated to be 18.245 keV and to be 22.0 keV, respectively, but not transmitted through the phase retarder system were incident on the sample crystals.

### 4.2. Sample crystal

Figure 4 is a reproduction of Fig 7 in reference [17] showing the experimental setup when the six-beam pinhole topographs shown in reference [17] were taken. Also in the case of $n$-beam pinhole topographs ($n \in \{3, 4, 5, 6, 8, 12\}$) the $[1\,\bar{1}\,1]$-oriented floating-zone silicon crystal with thickness 9.6 mm (for three-, four-, five-, six- and eight-beam topographs) and 10.0 mm (for twelve-beam topographs) were also mounted on the four-axis goniometer whose $\chi$-, $\phi$-, $\omega$- and $\theta$-axes can be rotated. Transmitted X-rays through the sample and two reflected X-rays were searched by three $PIN$ photo diodes as shown in Figure 4. The positions of the two $PIN$ photo diodes for detecting the reflected X-rays were determined using a laser beam guide reflected by a mirror. The mirror was mounted at the sample position on the goniometer whose angular positions were calculated such that the mirror reflects the laser beam to the direction of X-rays to be reflected by the sample crystal.

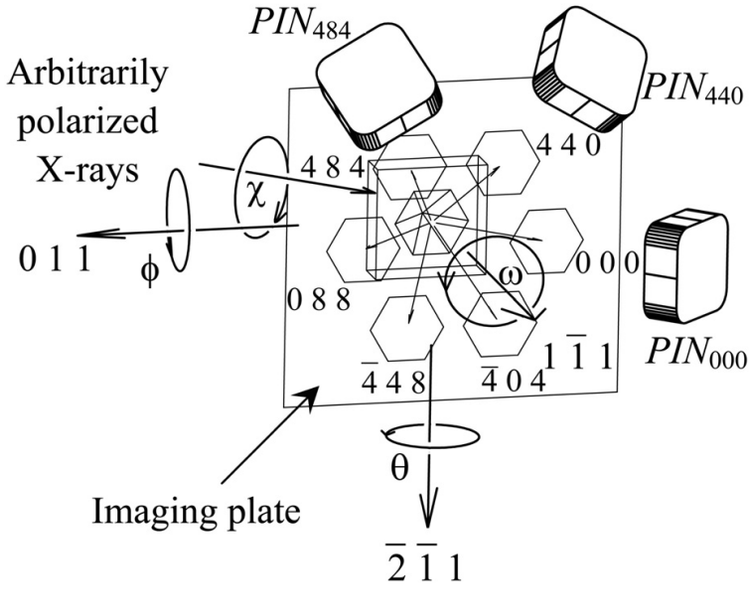


**Figure 4.** A schematic drawing of the goniometer on which the sample crystal was mount (reproduction of Figure 7 in reference [17]).

After adjusting the angular position of the goniometer such that the $n$-beam simultaneous reflection condition was satisfied, the size of slit $S$ in Figure 3 $(a)$ was limited to be $25\times25$ $\mu$m.

$N$ images of $n$-beam pinhole topographs were simultaneously recorded on an imaging plate placed behind the sample crystal.

## 5. Results and discussion

### 5.1. Three-beam case

Three-beam case is the most primitive case of X-ray multiple reflection. Figures 5[$E(a)$] and 5[$S(a)$] are 0 0 0-forward-diffracted and $\bar{4}$ 0 4- and 0 4 4-reflected X-ray pinhole topograph images. Figures 5[$E(b)$] and 5[$S(b)$] are enlargements of 0 4 4-reflected images from Figures 5[$E(a)$] and 5[$S(a)$], respectively. Fine-fringe regions ♯1 and ♯2 ([$FFR(1)$] and [$FFR(2)$]) and

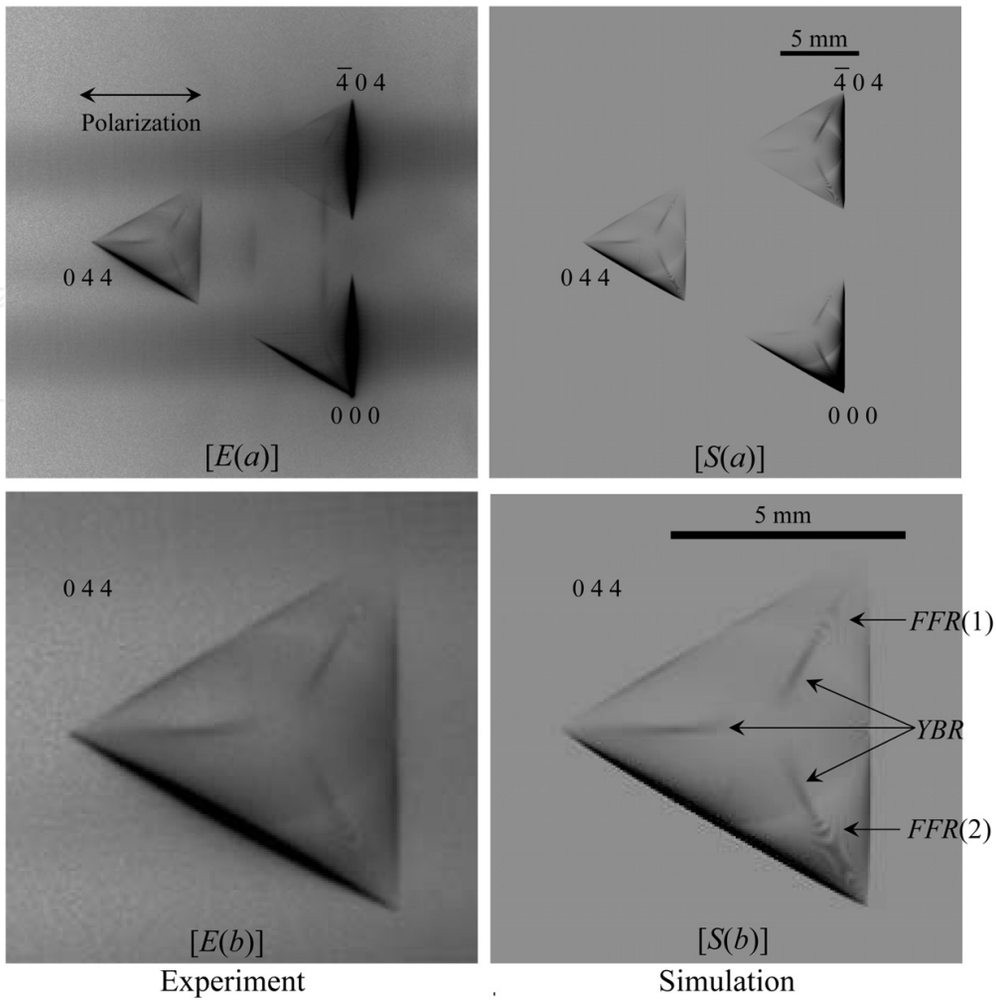


**Figure 5.** $[E(a)]$ and $[S(a)]$ $(x \in \{a, b\})$ are experimentally obtained and computer-simulated three-beam X-ray pinhole topographs with an incidence of horizontal-linearly polarized X-rays whose photon energy was 18.245 keV. $[Y(b)]$ $(Y \in \{E, S\})$ are enlargements of 0 4 4-reflected X-ray images in $[Y(a)]$. The exposure time for $[E(x)]$ was 600 s.

'Y-shaped' bright region ($YBR$) indicated by arrows in Figure 5$[S(b)]$, are found also in Figure 5$[E(b)]$.

## 5.2. Four-beam case

Figures $6[E(x)]$ and $6[S(x)]$ $(x \in \{a, b, c\})$ show experimentally obtained and computer-simulated pinhole topographs of 0 0 0-forward-diffracted, and 0 6 6-, $\overline{6}$ 2 8- and $\overline{6}$ $\overline{2}$ 4-reflected X-ray images, respectively. $[Y(a)]$, $[Y(b)]$ and $[Y(c)]$ $(Y \in \{E, S\})$ were obtained with an incidence of $+45°$-inclined-linearly, $-45°$-inclined-linearly and right-screwed-circularly polarized X-rays, respectively, generated with the phase retarder system or assumed in the simulation.

Figures $7[E(x)]$ and $7[S(x)]$ $(x \in \{a, b, c\})$ are enlargements of $\overline{6}$ 2 8-reflected X-ray images from Figures $6[E(x)]$ and $6[S(x)]$. In Figure $7[S(a)]$, fine-fringe region ♯1 $[FFR(1)]$, fine-fringe region ♯2 $[FFR(2)]$ and knife-edge line ($KEL$) are indicated by arrows. These characteristic patterns are also observed in Figure $7[E(a)]$. In Figures 7$[E(b)]$ and 7$[S(b)]$, while $FFR(2)$ is

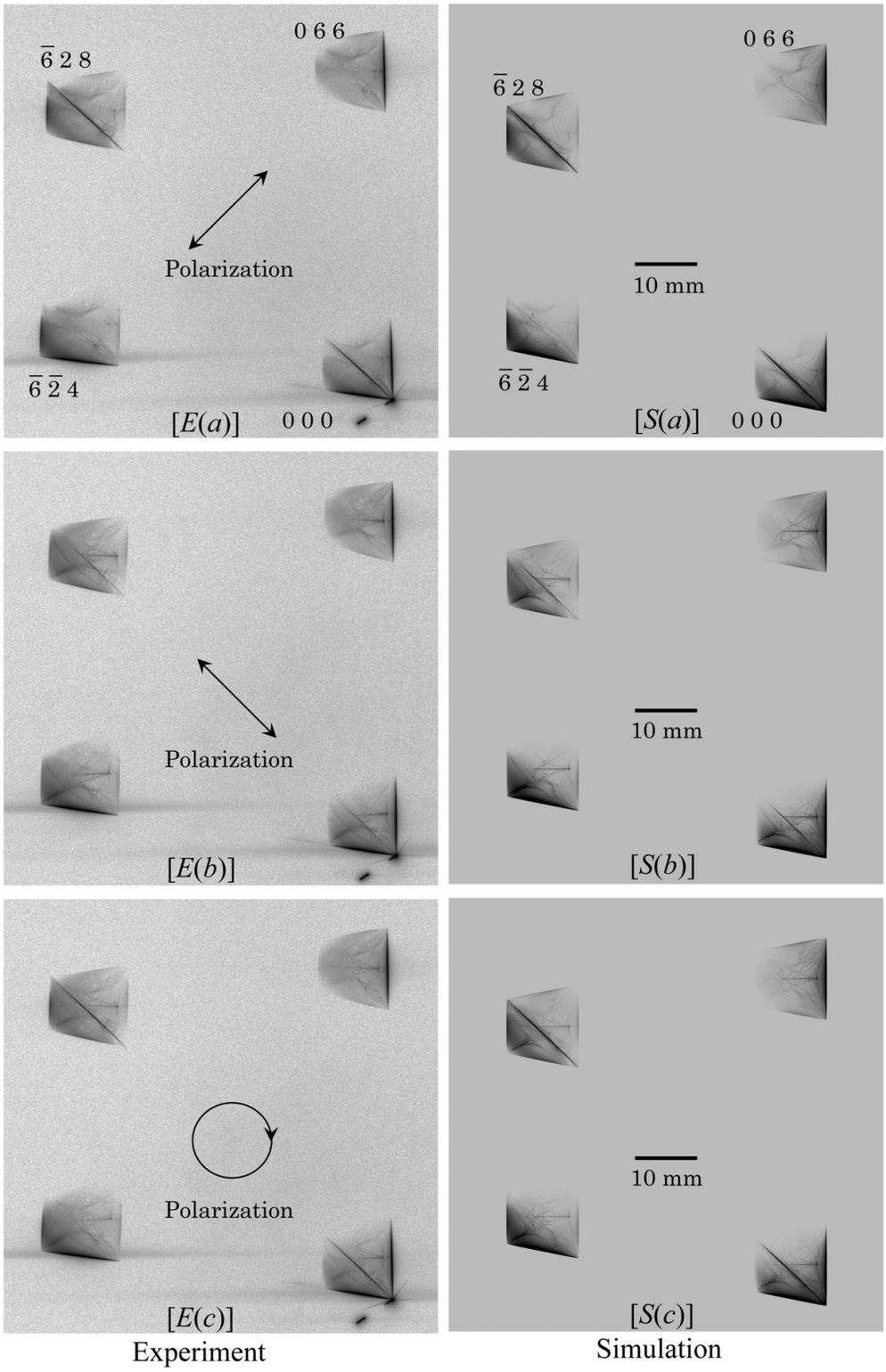


**Figure 6.** $[E(x)]$ and $[S(x)]$ $(x \in \{a, b, c\})$ are experimentally obtained and computer-simulated four-beam X-ray pinhole topographs with an incidence of $+45°$-inclined-linearly, $-45°$-inclined-linearly and right-screwed-circularly polarized X-rays whose photon energy was 18.245 keV. The exposure time for $[E(x)]$ was 1800 s.

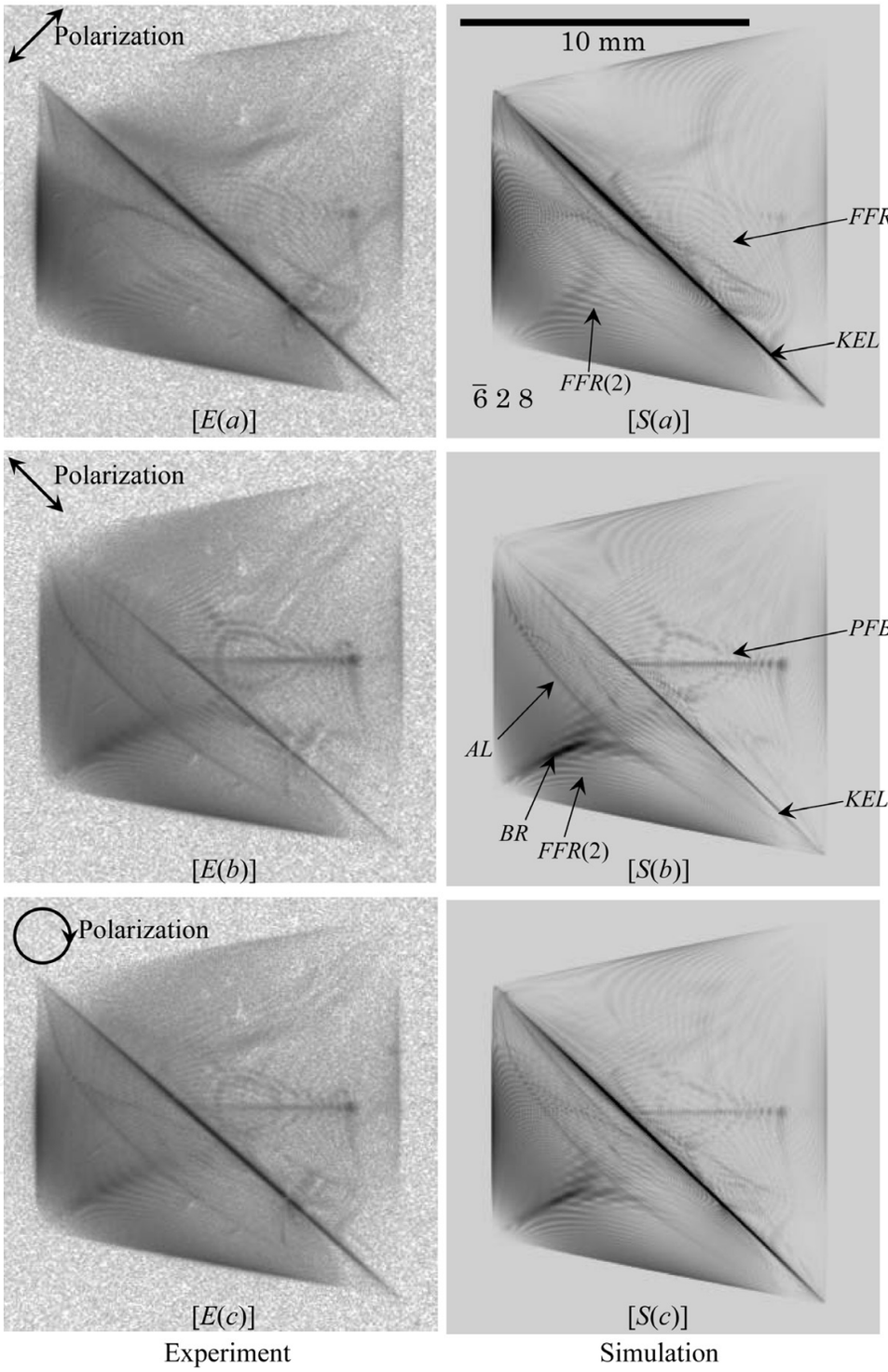


**Figure 7.** $[E(x)]$ and $[S(x)]$ ($x \in \{a, b, c\}$) are enlargements of $\overline{6}$ 2 8-reflected X-ray images in Figures 6 $[E(x)]$ and 6 $[S(x)]$.

observed at the same position, a pattern like a fish born ($PFB$) is observed in place of [$FFR(1)$]. $KEL$ in Figures 7[$E(b)$] and 7[$S(b)$] are fainter. Furthermore, an arched line ($AL$) and a bright region ($BR$) not observed in Figures 7[$E(a)$] and 7[$S(a)$] are observed in Figure 7[$E(b)$] and 7[$S(b)$]. In Figures 7[$E(c)$] and 7[$S(c)$], almost all the characteristic patterns above-mentioned are observed.

Between the horizontal and vertical components of incident X-rays, there is difference not in amplitude but in phase among Figures [$Y$(a)], [$Y$(b)] and [$Y$(c)] ($Y \in \{E, S\}$), which reveals that the wave fields excited by horizontal- and vertical-linearly polarized components of the incident X-rays interfere with each other.

### 5.3. Five-beam case

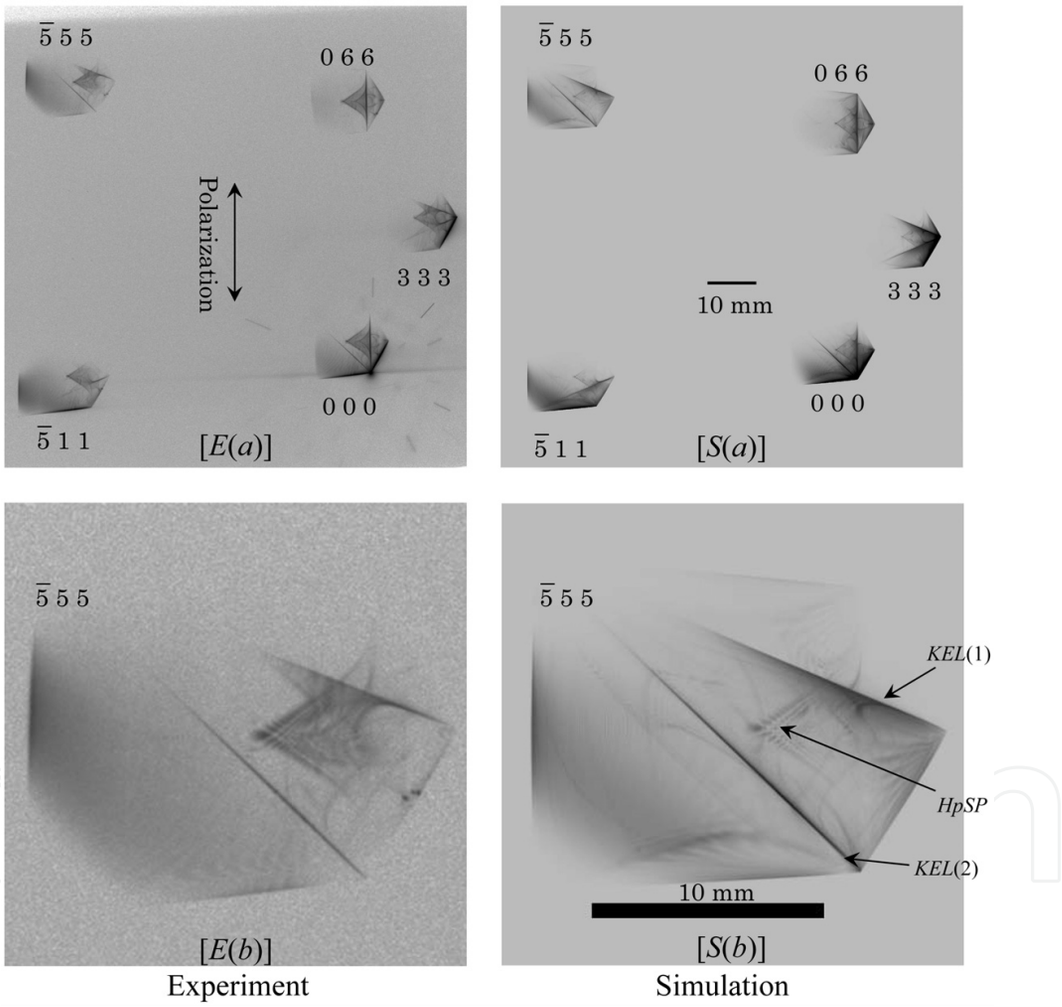


**Figure 8.** [$E(x)$] and [$S(x)$] ($x \in \{a, b\}$) are experimentally obtained and computer-simulated five-beam X-ray pinhole topographs with an incidence of vertical-linearly polarized X-rays whose photon energy was 18.245 keV. [$Y(b)$] ($Y \in \{E, S\}$) are enlargements of $\bar{5}$ 5 5-reflected X-ray images in [$Y(a)$]. The exposure time for [$E(x)$] was 1800 s.

In the case of cubic crystals, five reciprocal lattice nodes (including the origin of reciprocal space) can ride on a circle in reciprocal space. For understanding such a situation, refer to Figure 1 of reference [17].

Figures 8[$E(a)$] and 8[$S(a)$] are experimentally obtained and computer-simulated five-beam pinhole topographs. Figures 8[$E(b)$] and 8[$S(b)$] are enlargements of $\bar{5}$ 5 5-reflected X-ray images from Figures 8[$E(a)$] and 8[$S(a)$]. Knife-edge patterns ♯1 and ♯2 [$KEL(1)$ and $KEL(2)$] and 'harp-shaped' pattern ($HpSP$) indicated by arrows in Figure 8[$S(b)$] are observed also in Figure 8[$E(b)$].

Remarking on the directions of $KEL(1)$ and $KEL(2)$, these knife-edge patterns are directed to 0 0 0-forward-diffracted and 3 3 3-reflected X-ray images, respectively. Then, $KEL(1)$ and $KEL(2)$ are considered to suggest the strong energy exchange mechanism between 0 0 0-forward-diffracted and $\bar{5}$ 5 5-reflected X-ray wave fields and between 3 3 3- and $\bar{5}$ 5 5-reflected X-ray wave fields. Such knife-edge patterns are found also in three-, four-, six- and eight-beam pinhole topograph images shown in the present chapter.

## 5.4. Six-beam case

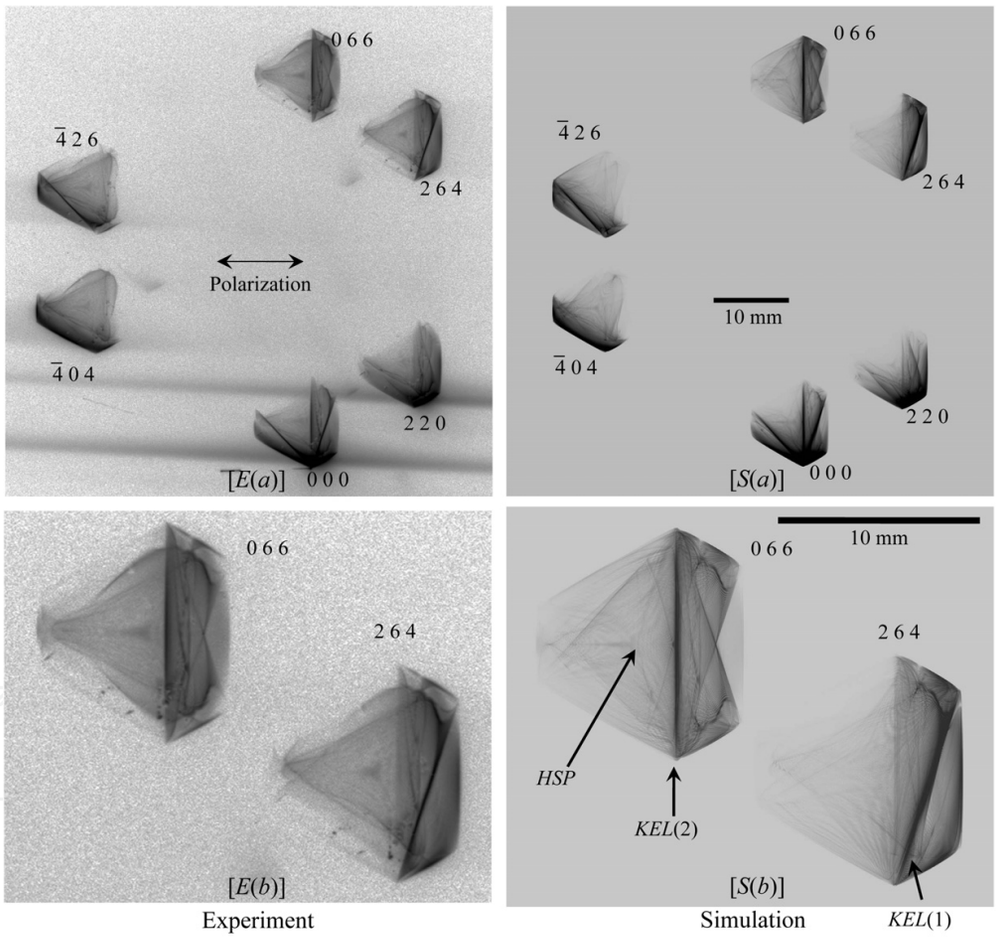


**Figure 9.** [$E(a)$] and [$S(a)$] are experimentally obtained and computer-simulated six-beam X-ray pinhole topographs with an incidence of horizontal-linearly polarized X-rays with a photon energy of 18.245 keV. [$E(b)$] and [$S(b)$] are enlargements of 2 6 4- and 0 6 6-reflected X-ray images in [$E(a)$] and [$S(a)$]. The exposure time for [$E(a)$] and [$E(b)$] was 300 s.

While experimental and computer-simulated six-beam pinhole topograph images whose shapes are regular hexagons have been reported in reference [14, 16, 17], shown in this

section are six-beam pinhole topographs whose Borrmann pyramid is not a regular hexagonal pyramid.

Such six-beam pinhole topographs experimentally obtained and computer-simulated are shown in Figure 9. Figures 9[$E(b)$] and 9[$S(b)$] are enlargements of 2 6 4- and 0 6 6-reflected X-ray images from Figures 9[$E(a)$] and 9[$S(a)$]. Knife-edge patterns [$KEL(1)$ and $KEL(2)$] indicated by arrows in Figure 9[$S(b)$] are found also in Figure 9[$E(b)$]. Circular patterns that were found in the central part of the six-beam pinhole topographs [14, 16, 17] cannot be found in the present case. A 'heart-shaped' pattern ($HSP$) is found also in Figure 9[$E(b)$].

### 5.5. Eight-beam case

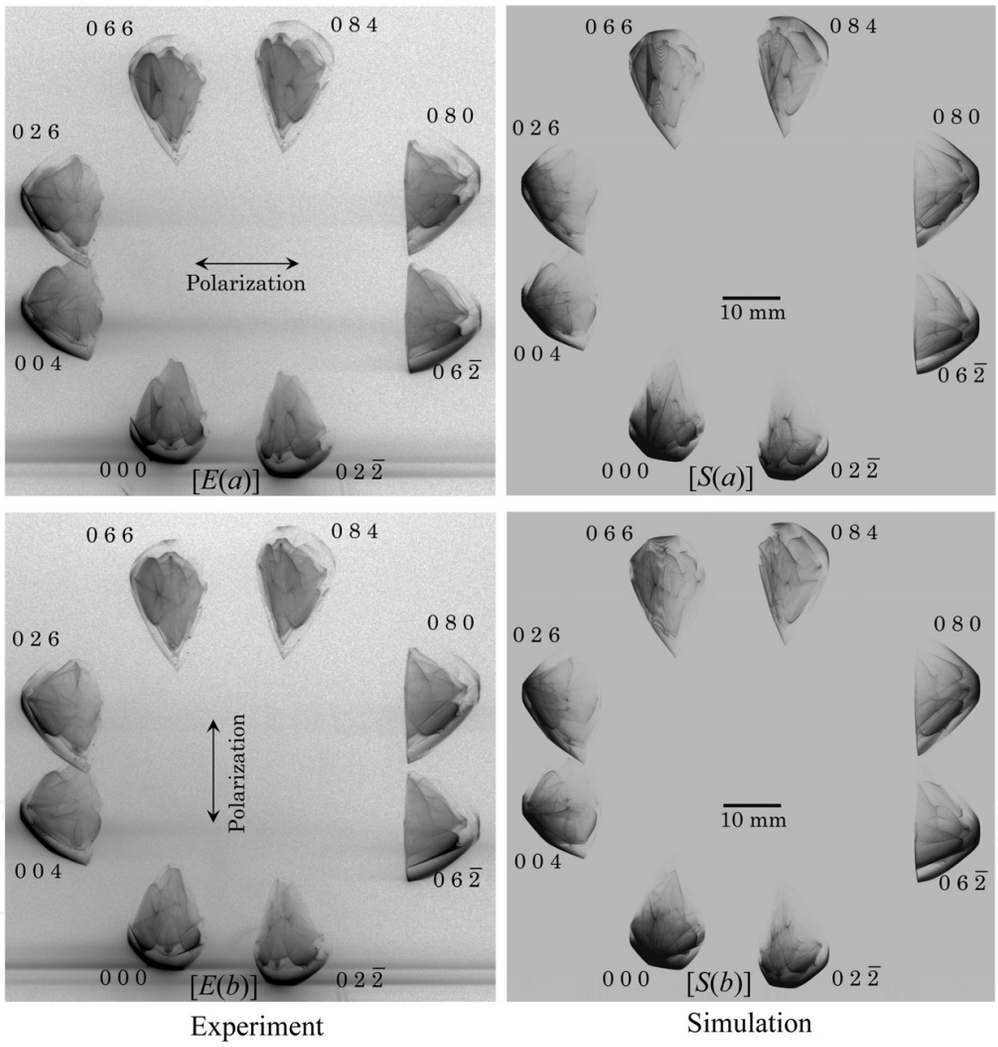


**Figure 10.** [$E(x)$] and [$S(x)$] ($x \in \{a, b\}$) are experimentally obtained and computer-simulated eight-beam X-ray pinhole topographs with an incidence of ($a$) horizontal-linearly and ($b$) vertical-linearly polarized X-rays whose photon energy was 18.245 keV. The exposure time for [$E(x)$] was 240 s.

Figure 10[$E(a)$] and 10[$S(a)$] are eight-beam X-ray pinhole topographs experimentally obtained and computer-simulated, respectively, with an incidence of horizontal-linearly

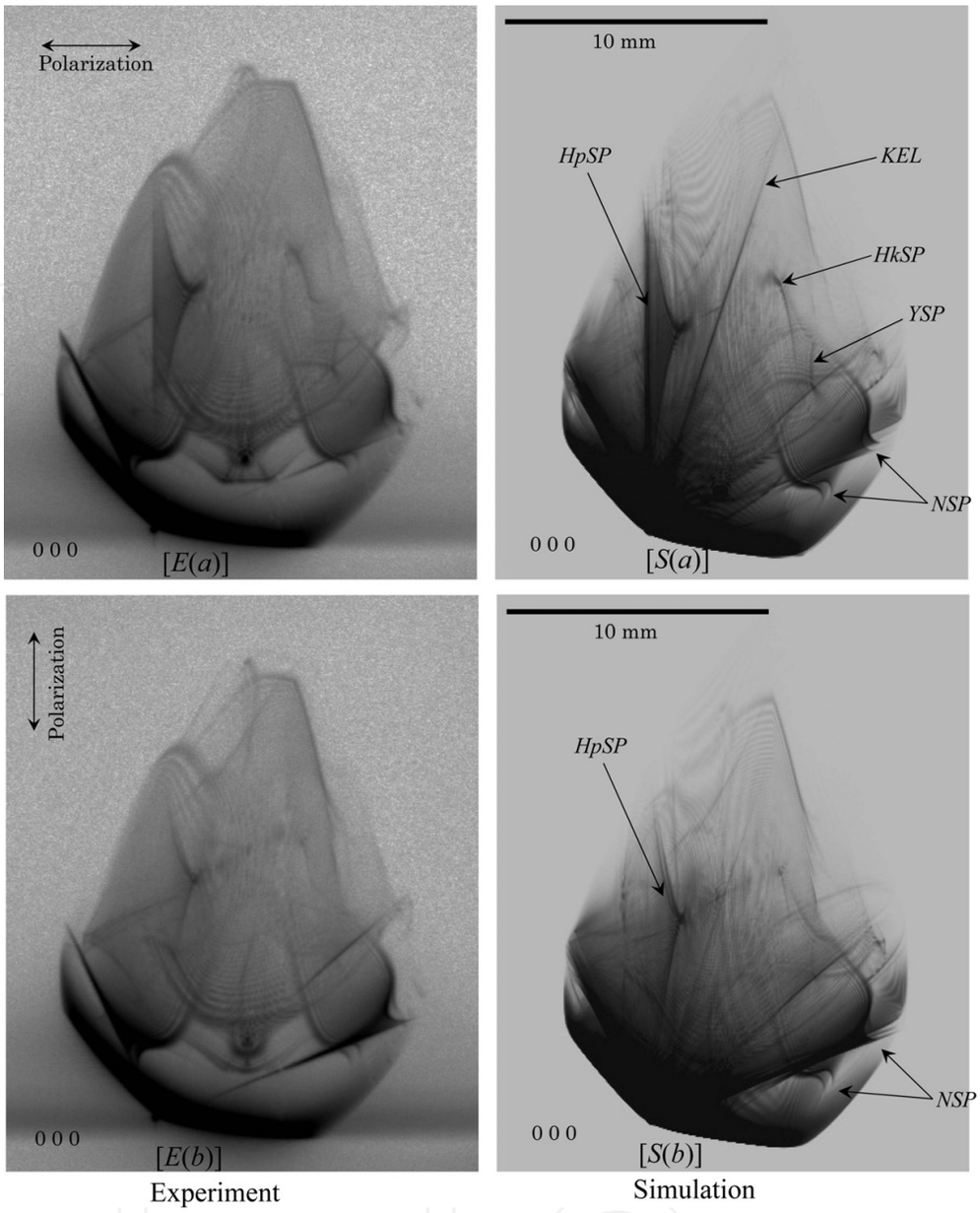


**Figure 11.** $[E(x)]$ and $[S(x)]$ $(x \in \{a, b\})$ are enlargements of 0 0 0-forward-diffracted X-ray images in Figures 10 $[E(x)]$ and 10 $[S(x)]$.

polarized X-rays. Figure 10$[E(b)]$ and 10$[S(b)]$ were obtained with an incidence of vertical-linearly polarized X-rays. Figure 11$[E(x)]$ and 11$[S(x)]$ $(x \in \{a, b\})$ are enlargements of 0 0 0-forward-diffracted X-ray images from Figures 10$[E(x)]$ and 10$[S(x)]$, respectively.

In Figure 11$[S(a)]$, A 'harp-shaped' pattern ($HpSP$), knife-edge line ($KEL$), 'hook-shaped' pattern ($HkSP$), 'Y-shaped' pattern ($YSP$) and 'nail-shaped' patterns are indicated by arrows. All these characteristic patterns are observed also in Figure 11$[E(a)]$. $NSP$ is also observed in Figures 11$[E(b)]$ and 11$[S(b)]$. However, $HpSP$ in Figures 11$[E(b)]$ and 11$[S(b)]$ are rather fainter compared with Figures 11$[E(a)]$ and 11$[S(a)]$.

### 5.6. Twelve-beam case

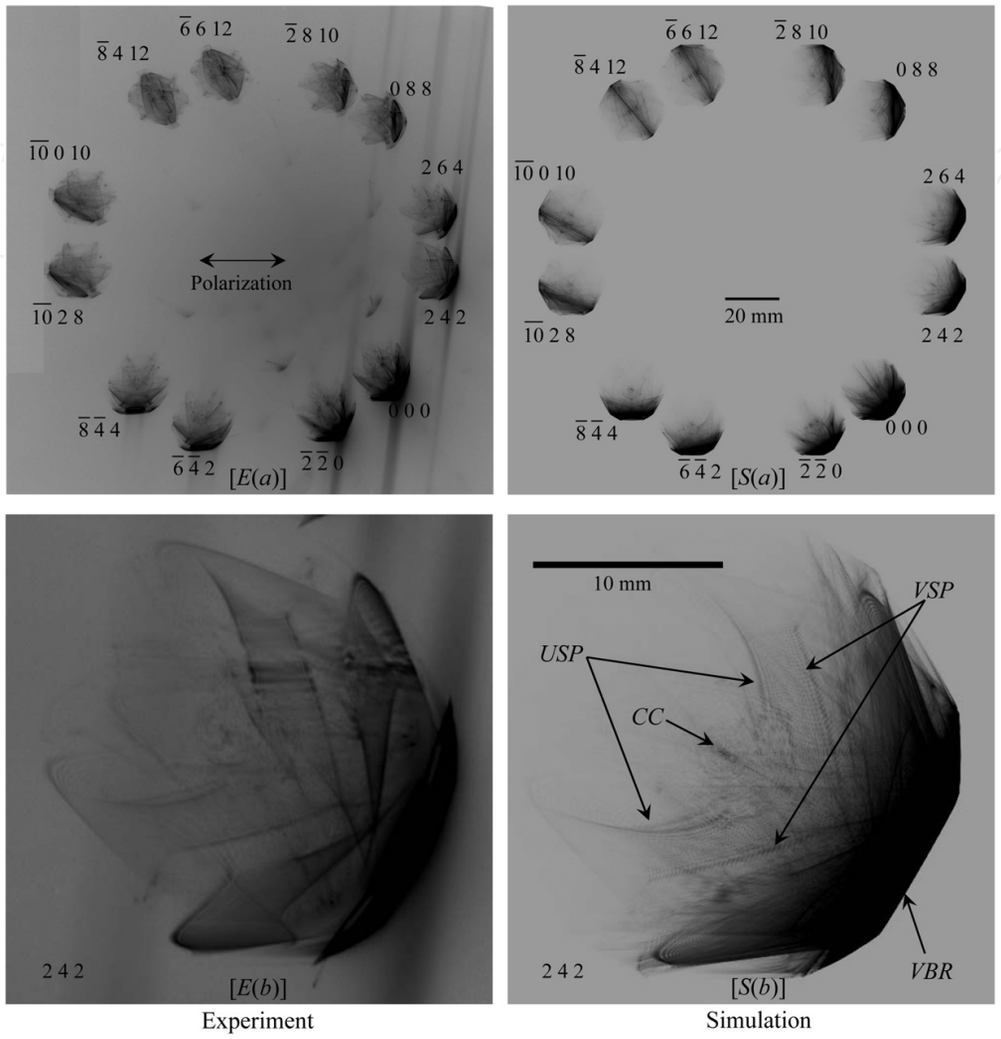


**Figure 12.** $[E(a)]$ and $[S(a)]$ are experimentally obtained and computer-simulated twelve-beam X-ray pinhole topographs with an incidence of horizontal-linearly polarized X-rays whose photon energy was 22.0 keV. $[E(b)]$ and $[S(b)]$ are enlargements of 2 4 2-reflected X-ray images in $[E(a)]$ and $[S(a)]$. The exposure time for $[E(a)]$ and $[E(b)]$ was 300 s.

Twelve is the largest number of $n$ for the $n$-beam T-T equation (14) that restricts a condition that $n$ reciprocal lattice nodes should ride on a circle in reciprocal space. Figures 12$[E(a)]$ and 12$[S(a)]$ are experimentally obtained and computer-simulated tweleve-beam pinhole topographs. Figures 12$[E(b)]$ and 12$[S(b)]$ are enlargements of 2 4 2-reflected X-ray images from Figures 12$[E(a)]$ and 12$[S(a)]$.

A very bright region ($VBR$), 'V-shaped' pattern ($VSP$), central circle ($CC$) and 'U-shaped' pattern indicated by arrows in Figure 12$[S(b)]$ are found also in Figure 12$[E(b)]$.

## 6. Summary

The $n$-beam ($n \in \{3, 4, 5, 6, 8, 12\}$) Takagi-Taupin equation and computer algorithm to solve it were verified from excellent agreements between experimentally obtained and computer-simulated three-, four-, five-, six-, eight- and twelve-beam pinhole topographs.

The equivalence between the E-L and T-T formulations of the $n$-beam X-ray dynamical diffraction theory, which has been implicitly recognized for two-beam case theory, was explicitly described in the present chapter. Whereas the former theory can be calculated by solving an eigenvalue-eigenvector problem, the latter can be calculated by solving a partial differential equation. This equivalence is very similar to that between the Heisenberg and Schrödinger pictures of quantum mechanics and is very important.

Whereas this chapter has been described with focusing on the $n$-beam case that $n \in \{3, 4, 5, 6, 8, 12\}$, the $n$-beam X-ray dynamical diffraction theory applicable to the case of arbitrary number of $n$, which is effective and important for solving the phase problem in protein crystal structure analysis, will be described elsewhere. In the case of protein crystallography, the situation that arbitrary number of reciprocal lattice nodes are very close to the surface of the Ewald sphere, cannot be avoided. In protein crystallography, the $n$-beam X-ray dynamical diffraction theory for arbitrary number of $n$ is necessary.

## Acknowledgements

The part of theoretical study and computer simulation of the present work was conducted in Research Hub for Advanced Nano Characterization, The University of Tokyo, supported by the Ministry of Education, Culture, Sports, Science and Technology (MEXT), Japan.

HITACHI SR-11000 and SGI Altix ICE 8400EX super computer systems of the Institute for Solid State Physics of The University of Tokyo were used for the computer simulations.

The preliminary experiments were performed at AR-BL3A of the Photon Factory AR under the approval of the Photon Factory Program Advisory Committee (Proposals No. 2003G202 and No. 2003G203). The main experiments were performed at BL09XU of SPring-8 under the approval of Japan Synchrotron Radiation Research Institute (JASRI) (Proposals No. 2005B0714 and No. 2009B1384).

The present work is one of the activities of Active Nano-Characterization and Technology Project financially supported by Special Coordination Fund of the Ministry of Education, Culture, Sports, Science and Technology of the Japan Government.

The authors are indebted to Dr. Y. Ueji Dr. X.-W. Zhang and Dr. G. Ishiwata for their technical support in the present experiments and also to Professor Emeritus S. Kikuta for his encouragements and fruitful discussions for the present work.

## Author details

Kouhei Okitsu
*Nano-Engineering Research Center, Institute of Engineering Innovation, Graduate School of Engineering, The University of Tokyo, 2-11-16 Yayoi, Bunkyo-ku, Tokyo 113-8656, Japan*

Yasuhiko Imai and Yoshitaka Yoda
*Japan Synchrotron Radiation Research Institute, SPring-8, 1-1-1 Kouto, Mikazuki-cho, Sayo-gun, Hyogo 679-5198, Japan*

## 7. References

[1] Authier, A. [2005]. *Dynamical Theory of X-Ray Diffraction, Reprinted with Revisions 2004, 2005.*, Oxford University Press.
[2] Chang, S.-L. [2004]. *X-Ray Multiple-Wave Diffraction, Theory and Application*, SPringer.
[3] Colella, R. [1974]. *Acta Cryst.* A30: 413–423.
[4] Colella, R. [1995a]. *Comments Cond. Mat. Phys.* 17: 175–198.
[5] Colella, R. [1995b]. *Comments Cond. Mat. Phys.* 17: 199–215.
[6] del Rio, M. S. & Dejus, R. J. [1998]. *Proc. SPIE* 3448: 340–345.
[7] Ewald, P. P. [1917]. *Ann. Phys. 4. Folge* 54: 519–597.
[8] Ewald, P. P. & Héno, Y. [1968]. *Acta Cryst.* A24: 5–15.
[9] Héno, Y. & Ewald, P. P. [1968]. *Acta Cryst.* A24: 16–42.
[10] Hildebrandt, G. [1967]. *Phys. Stat. Sol.* 24: 245–261.
[11] Laue, M. v. [1931]. *Ergeb. Exakten Naturwiss* 10: 133–158.
[12] Lipscomb, W. N. [1949]. *Acta Cryst.* 2: 193–194.
[13] Okitsu, K. [2003]. *Acta Cryst.* A59: 235–244.
[14] Okitsu, K., Imai, Y., Ueji, Y. & Yoda, Y. [2003]. *Acta Cryst.* A59: 311–316.
[15] Okitsu, K., Ueji, Y., Sato, K. & Amemiya, Y. [2002]. *Acta Cryst.* A58: 146–154.
[16] Okitsu, K., Yoda, Y., Imai, Y. & Ueji, Y. [2011]. *Acta Cryst.* A67: 550–556.
[17] Okitsu, K., Yoda, Y., Imai, Y., Ueji, Y., Urano, Y. & Zhang, X.-W. [2006]. *Acta Cryst.* A62: 237–247.
[18] Takagi, S. [1962]. *Acta Cryst.* 15: 1311–1312.
[19] Takagi, S. [1969]. *J. Phys. Soc. Jpn.* 26: 1239–1253.
[20] Taupin, D. [1964]. *Bull. Soc. Fr. Minéral. Cristallogr.* 87: 469–511.
[21] Weckert, E. & Hümmer, K. [1997]. *Acta Cryst.* A53: 108–143.
[22] Weckert, E. & Hümmer, K. [1998]. *Cryst. Res. Technol.* 33: 653–678.